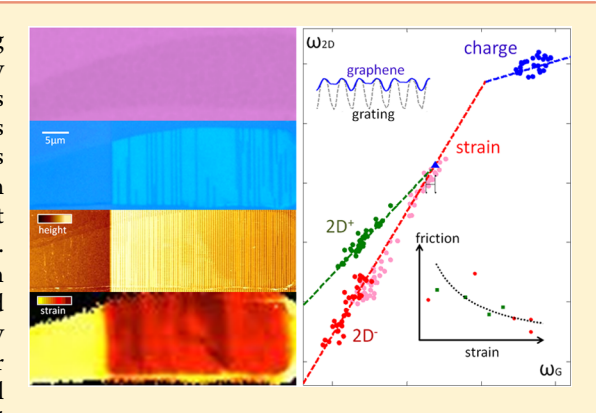


Uniaxial Strain Redistribution in Corrugated Graphene: Clamping, Sliding, Friction, and 2D Band Splitting

Xuanye Wang,[†] Khwanchai Tantiwanichapan,[†] Jason W. Christopher,[‡] Roberto Paiella,^{†,+} and Anna K. Swan*,†,‡,+

Supporting Information

ABSTRACT: Graphene is a promising material for strain engineering based on its excellent flexibility and elastic properties, coupled with very high electrical mobility. In order to implement strain devices, it is important to understand and control the clamping of graphene to its support. Here, we investigate the limits of the strong van der Waals interaction on friction clamping. We find that the friction of graphene on a SiO₂ substrate can support a maximum local strain gradient and that higher strain gradients result in sliding and strain redistribution. Furthermore, the friction decreases with increasing strain. The system used is graphene placed over a nanoscale SiO2 grating, causing strain and local strain variations. We use a combination of atomic force microscopy and Raman scattering to determine the friction coefficient, after accounting for compression and accidental charge doping, and model the local strain variation within the laser spot size. By using uniaxial



strain aligned to a high crystal symmetry direction, we also determine the 2D Raman Grüneisen parameter and deformation potential in the zigzag direction.

KEYWORDS: graphene, strain engineering, friction, corrugated surface, Raman spectroscopy, 2D mode Grüneisen parameter

The measurements over a decade ago of graphene's remarkable electronic structure has opened new exciting areas of research with graphene and other 2D materials and the possibility of flexible electronics.^{2,3} The mechanical properties of graphene are also outstanding. The strong carbon-carbon bond makes it as stiff as diamond with a similar Young's modulus, whereas the high perfection of the lattice yields a remarkably high elastic region of over 20% bond elongation.⁴ These properties, combined with the remarkably high mobility of graphene Dirac Fermions, have inspired several strain engineering proposals⁵ and devices, such as confinement and electron beam collimation in 1D channels, 6 changing the electronic structure for graphene supported on pillars, opening of an energy bandgap in strain superlattices,8 and the generation of strain-induced pseudomagnetic fields with resulting Landau level quantization. 9,10 For such strain devices as well as graphene membrane resonators, 11,12 it is important to have strong clamping boundary conditions. Hence, the friction is of importance, an area starting to be addressed both theoretically 13 and experimentally. $^{14-16}$ The strong van der Waals forces 17 and the flexibility of graphene produce good conformation even to a microscopically structured surface like SiO₂, which provides reasonably good frictional force that is

able to clamp graphene in place. However, in some cases it is also possible to envision the benefit of low friction, for example, to allow graphene to slide in order to prepare well conformed and strain free corrugated graphene for terahertz generation via cyclotron-like radiation. 19

In previous work¹⁴ using pressurized suspended graphene, we reported that graphene slides under radial strain and that the friction coefficient can be determined and is strain dependent. In this study we investigate the interplay between uniaxial strain, friction, and sliding/clamping of graphene and find that there is a maximum strain variation per length $(\Delta \varepsilon/L)$ that can be sustained for a given friction and that the friction decreases inversely with strain. The upper limit on $(\Delta \varepsilon/L)$ is caused by graphene sliding, which lessens strain variations. Here, uniaxial strain is created in graphene transferred to a sinusoidal SiO2 grating and adjacent flat area, which is held in place by van der Waals forces. The grating induces uniaxial tensile strain because of its longer surface length along the corrugation (relative to a flat region of equal extent), such that

Received: May 28, 2015 Revised: July 2, 2015 Published: July 28, 2015

5969

Department of Electrical and Computer Engineering, Boston University, 8 St. Mary's Street, Boston, Massachusetts 02215, United

^{*}Department of Physics, Boston University, 590 Commonwealth Avenue, Boston, Massachusetts 02215, United States

[†]Photonics Center, Boston University, 8 St. Mary's Street, Boston, Massachusetts 02215, United States

when flat graphene is deposited onto the grating, it needs to elongate to conform to the underlying structure. The friction as a function of strain on the grating is the same as on the flat substrate, indicating that the gentle grating corrugation does not affect the friction. We use atomic force microscopy (AFM) to determine the physical corrugation of the graphene on the grating, which gives a geometric estimate of the average strain based on the length of the sinusoidal shape assuming no sliding. In the Raman data analysis, the 2D and G bands are first used to separate the strain and charge contributions to the peak positions²⁰⁻²⁴ and then to determine the strain and the strain dependent friction coefficient. We find a finite strain gradient region between the flat surface and the grating and a weakly varying strain over the grating area. Furthermore, the average strain in the grating region is found to be lower than the aforementioned geometric estimate. These results indicate that the strain gradient is limited by the friction and that graphene slides into the strained region, reducing the average strain. Using an elastic model and the local strain and strain gradient, we then evaluate the friction between graphene and SiO₂ for single and double layer graphene and obtain a coherent picture of decreasing friction with increasing uniaxial strain. The friction can support a maximum local strain difference, with higher strain gradients resulting in the observed sliding and strain redistribution. An upper bound of the local strain variation within the laser diffraction limited spot is determined from the G⁻ band line width, which matches well with the result from the elastic model. Furthermore, by using uniaxial strain aligned to a high crystal symmetry direction, we also determine the 2D Raman Grüneisen parameter and the shear deformation potential in the zigzag direction. Other findings from our measurements are the compression of graphene on flat SiO₂ ($\varepsilon = -0.11 \pm 0.02\%$), as well as the degree of spatial variation in the accidental charge doping, $2-4 \times 10^{12}$ cm⁻² on the flat SiO_2 and $<10^{12}$ cm⁻² on the grating.

To achieve a sinusoidal substrate grating profile, $A_0 \sin(2\pi x/$ Λ_0), we introduce a novel wet etch and two-step thermalgrowth fabrication process. A schematic view of this process is shown in Figure 1. A Si(100) surface is first patterned by electron beam lithography with Cr stripes of width $W = (\Lambda_0/2)$ - $2A_0\sin(54.74^\circ)$ repeated with periodicity Λ_0 . A highly anisotropic wet etch in KOH is then used to produce a periodic pattern of trapezoidal ridges with (111)-oriented sidewalls.²⁵ Next, the sample is thermally oxidized for 5 h at 1100 °C, and as a result, the buried Si/SiO₂ interface develops a smooth, highly rounded morphology (which is attributed to different oxidation rates near the sharp corners of the Si ridges²⁶). In particular, with the aforementioned choice for the Cr stripe width W, we obtain a highly sinusoidal grating, as revealed by AFM imaging. Finally, a second thermal growth is performed in order to coat the corrugated Si surface with a (280 nm thick) conformal SiO2 layer. The specific grating samples used in this work have period Λ_0 = 400 nm and peak-to-peak amplitude $2A_0$ = 55 nm. The microscopic roughness on the flat and corrugated substrate is typical for SiO₂, 0.2-0.4 nm RMS.

Single-layer mechanically exfoliated graphene is then deposited onto the sinusoidal grating by a pick-and-place transfer method. A schematic view of this graphene deposition method can be seen in the Supporting Information, Figure S1. Graphene is first exfoliated onto a layer of the water-soluble polymer polyvinylpyrrolidone (PVP) deposited on a Si substrate, with thickness optimized for color contrast to aid optical visualization. A transparent polydimethylsiloxane

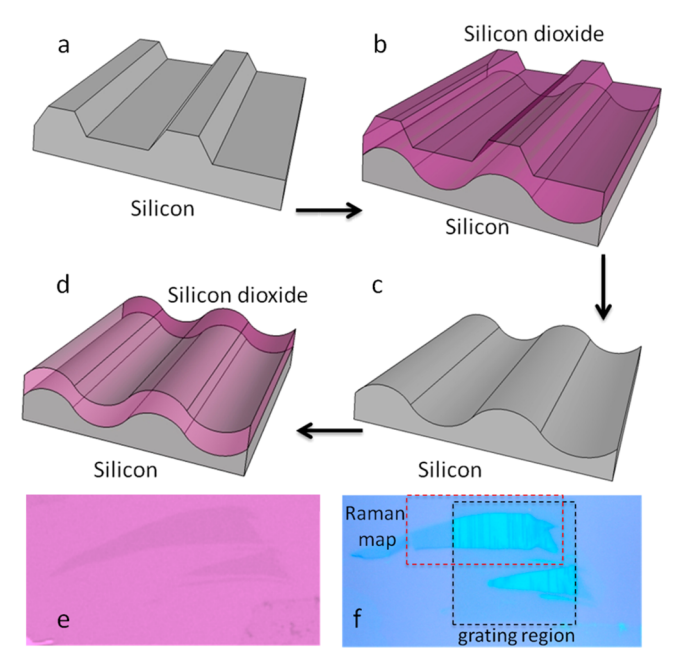


Figure 1. Schematic illustration of the wet etch and two-step thermal-growth process used for fabricating sinusoidal SiO₂ gratings, and optical images of the graphene sample studied in this work before and after transfer to a grating. (a) Silicon substrate after electron beam lithography and anisotropic KOH etch. (b) Grating sample after the first thermal oxidization step leading to the formation of a smooth Si/SiO₂ buried interface. (c) Grating sample after SiO₂ removal with HF to reveal the sinusoidal surface corrugation. (d) Grating sample after the final thermal oxidization growth. (e) Graphene flakes on PVP/Si substrate before transfer. (f) Graphene flakes after transfer to a grating. The grating and Raman mapping regions are indicated by the dashed boxes.

(PDMS) block with a thermal release layer of methyl methacrylate (MMA) is then attached to the PVP film over the graphene. After dissolving the PVP in water, the graphene layer is picked up by the PDMS block, which can be manipulated with a standard translational stage under a microscope. With this setup, the graphene layer is then aligned and released onto the grating region by pressing it against the substrate and heating the sample to 100 °C, beyond the glass-transition temperature of MMA. Standard cleaning by acetone and deionized water is finally applied. This transfer technique is similar to other reported methods.²⁷

As shown in Figure 1f, the graphene sample transferred to the grating and described in the following consists of two adjacent flakes, with the long edge of the larger flake aligned perpendicular to the grating lines. Both flakes have similar lattice orientation and strain behavior. Polarized Raman data (Supporting Information, Figures S3 and S9) show that the strain induced in these two flakes is uniaxial along a direction at an angle $\varphi = 5.0^{\circ} \pm 0.3^{\circ}$ and 3.5° , respectively, with the zigzag lattice direction. These angles are sufficiently small so that we can treat the strain as aligned with the zigzag direction in the subsequent data analysis.

The graphene has been profiled with AFM to measure its conformation to the grating. Comparison between the optical image of Figure 2a and the AFM map of Figure 2c shows that the sample regions imaged in the lighter blue color correspond to graphene with an average sinusoidal corrugation amplitude $2A \sim 20$ nm, with variations from 18 to 25 nm. The dark lines correspond to regions where graphene is partially suspended

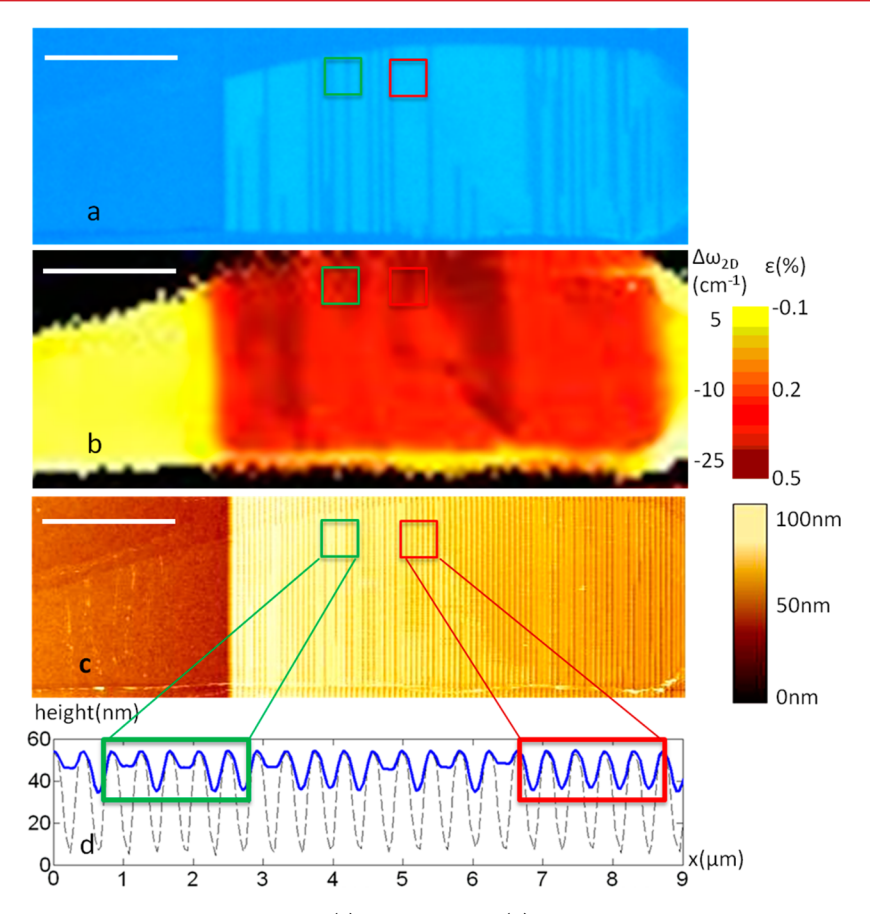


Figure 2. Graphene flake on a SiO_2 grating. Scale bar: $10 \mu m$. (a) Optical image. (b) Map of Raman 2D-band peak center position. (c) AFM height map. (d) AFM line scan. The darker regions in (a) correspond to grating lines with partially flat graphene, as can be clearly seen in (d). The red and green boxes correspond to regions of good conformation and partial suspension, respectively.

with ~ 5 nm height variation. We note that a molecular dynamics simulation of flat graphene films deposited onto a corrugated surface²⁸ finds very similar attachment patterns. In these calculations, regions of partially suspended graphene are found in between well conforming sections for similar ratio of period to amplitude of the grating $((\Lambda_0/(A_0)=14.5)$, albeit with order of magnitudes smaller dimensions.

As the graphene flake is deposited onto the grating, we can imagine a flat sheet first attaching to the top of the grating lines without any induced strain. Assuming perfect clamping, further adhesion would result in an elongation of the sheet by the amount $\Delta L \approx (\pi A)^2/\Lambda$ per period, with maximum strain at the location of the troughs. Thus, instead of having a uniform average value $\overline{\varepsilon}$, the strain in each period would vary sinusoidally between 0 at the top and $2\overline{\varepsilon}$ at the bottom of the grating. The strain difference per unit length is then given by $((\Delta \varepsilon)/(\Delta x)) = 2\overline{\varepsilon}/(\Lambda_0/2)$ (Supporting Information, Figure S6). Using the AFM line profiles, such as the example shown in Figure 2d, we can estimate the average strain $\overline{\varepsilon}$ from the period Λ_0 and amplitude A of the graphene corrugation, that is, $\overline{\varepsilon}$ = $\Delta L/\Lambda_0 \approx (\pi A/\Lambda_0)^2$. Using the average measured graphene amplitude 2A = 20 nm, we find $\overline{\varepsilon} = 0.62\%$, whereas the minimum and maximum corrugation values of 18 and 25 nm result in a geometrical strain of 0.5 to 0.9%, respectively. On the basis of the same analysis, the graphene regions in the dark lines of Figure 2a are expected to have a lower average strain of $\sim 0.15\%$

The 2D Raman mapping in Figure 2b shows the strain variations between different areas, and how they correspond to

the degree of conformation. Note that the highly conformed graphene is less strained than the geometric approximation, whereas the graphene in the dark region is more strained than expected. Both observations are consistent with a picture of graphene partially sliding over the grating, causing a redistribution and homogenization of the induced strain. Graphene on the flat silicon dioxide substrate is determined from the analysis below to be compressed by 0.11% (yellow color). Furthermore, there is a \sim 3 μm wide transition region on the flat substrate next to the grating where the 2D peak rapidly downshifts. These results demonstrate that the van der Waals forces are not strong enough to fully clamp the graphene on the flat area and that graphene close to the grating is sliding inward. We obtained similar result for pressurized graphene over small chambers. 14 The strain value stabilizes after the first grating period. This result was observed on all samples studied (Supporting Information).

Before using the Raman G^- peak position and G^- line width to analyze the strain and strain distribution in more detail, we need to disentangle strain contributions to line width and peak shifts from those due to charge. It is well known from transport studies that standard transfer techniques of graphene to SiO_2 substrates causes substantial accidental p-doping, 29 which also shifts the G and 2D peaks. 20,21,23 We use the relationship between the 2D and 2D peak positions to graphically and statistically separate charge and strain contributions by analyzing the slope of the 2D versus 2D data.

For this purpose, Raman data were acquired using a 532 nmwavelength linearly polarized laser. Figure 3 shows the

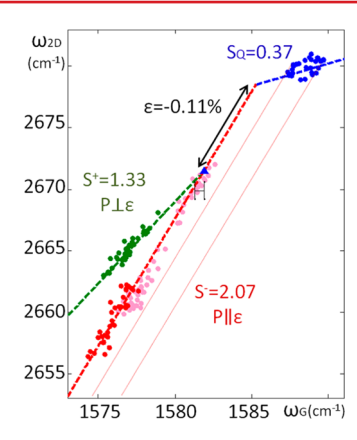


Figure 3. Correlation between the measured $2D^{\pm}$ - and G-band peak positions. Both peaks shift with charge as well as strain. The red, violet, and green data are from the grating region; the blue points are from the flat substrate area. The lines are fit to the data and indicate the $2D^-/G$ strain ratio (red) S^- 2.07 \pm 0.36, the $2D^+/G$ strain ratio (green) S^+ = 1.33 \pm 0.14, and the 2D/G charge slope (blue) S_Q = 0.37 \pm 0.28. The red and violet data were measured from two different graphene flakes. The graphene on the flat surface is compressed by \sim 0.11 \pm 0.02%, as indicated by the black double arrow. The dotted red lines correspond to a charge density $n \sim 2 \times 10^{12}$ cm⁻² and 4×10^{12} cm⁻².

correlation between the 2D and G band peak centers at different locations on the sample. The blue data points are from graphene on the flat area outside the grating, and the red points are from the grating area of sinusoidally conformed graphene with the laser light polarized along the strain direction. The green points are from the partially conformed graphene (the dark lines in Figure 1a) with the laser polarization perpendicular to the strain direction. It is apparent from Figure 3 that there are qualitatively different behaviors in the grating and flat substrate. The data points from the strained graphene (red and green) fall tightly along steep lines with slopes S^{\pm} , whereas the data points from the flat graphene (blue) are clustered with a lower slope S_Q . Following the analysis from Lee et al., ²⁴ any point away from the intrinsic value $(\omega_{G_2}\omega_{2D_2})$ can be decomposed into a strain vector and a charge vector, so that a point (ω_{G},ω_{2D}) can be assigned with separate charge and strain components. As explained in the following, the higher slopes S^{\pm} are associated with strain variation, and the lower slope S_Q with charge variation.

The two straight lines of slopes S^{\pm} intersect at $(\omega_{G_0}, \omega_{2D_0}) =$ (1581.9 cm⁻¹, 2671.5 cm⁻¹), which we take as the zero-strain G-band Raman peak position (triangle pointing up). This is very close to the adjusted value found on suspended graphene,²⁴ (Supporting Information section 4.3) $(\omega_{G_0}',\omega_{2D_0}')$ = $(1581.6 \pm 0.2 \text{ cm}^{-1}, 2669.9 \pm 0.7 \text{ cm}^{-1})$, also indicated in the figure (error bar below $(\omega_{G_0}, \omega_{2D_0})$). The linear fits to the data give slope $S^- = 2.07 \pm 0.36$ and $S^+ = 1.33 \pm 0.14$. Our measured value of S⁻ is similar to the strain slope reported earlier²⁴ (S = 2.2), although the sample configuration here is different. In particular, in the work by Lee et al. 24 the strain and compression slope was given by an average of randomized strain and polarization directions, which did not allow for a direct comparison between measured and calculated values. The data from the flat substrate has more spread, but it is clear that the slope is lower, $S_Q = 0.37 \pm 0.28$. The larger relative uncertainty of S_Q is due to the larger spread of the blue points, indicating that there are both local charge and compression variations of comparable magnitude on the flat substrate, similar to previous results.²⁴ We also note that S_O here is substantially lower than the value $S_{\rm O} = 0.75$ obtained by Lee et al.,24 but they were considering significantly higher doping levels. To explain this difference, we use the measurements by Das et al.²³ on monolayer graphene on SiO₂ to extract the 2D peak shift with charge, combined with the known G band variation with charge. 23 The G band shift with charge is linear for $|E_F| > ((E_\omega G)/2) = 0.1 \text{ eV or } n > 0.6 \times 10^{12} \text{ cm}^{-2}$, whereas the 2D band varies linearly with charge up to $\sim 6 \times 10^{12}$ cm⁻², above which the slope increases sharply.²³ Hence, for the regime $[0.6-6] \times 10^{12}$ cm⁻², the charge vector $(\Delta \omega_{\rm G}, \Delta \omega_{\rm 2D})_{\rm O}$ is linear, and we extract a slope $S_Q = 0.25$ (Supporting Information, Figure S8.) This is close to our measured value (0.37 ± 0.28) , especially considering the uncertainties in the extracted slope from the aforementioned published data²³ and the uncertainty in determination the charge slope discussed

The origin of the two strain slopes S^{\pm} is related to the splitting of the two 2D[±] components under uniaxial strain along a high symmetry direction of the lattice.³⁰ In our sample, the strain and zigzag directions are closely aligned (within 5°), and therefore, we can expect a visible split of the two 2D[±] Raman peaks. The two polarization directions of the laser light used in our measurements (parallel and perpendicular to the strain and zigzag direction) select the two different 2D± components. In particular, only the 2D component is selected when the polarization is parallel to the strain and zigzag direction, $P||\varepsilon||zz$. This is the case for the red data points of Figure 3, and therefore, the corresponding slope is named S^- . Vice versa, when the polarization is perpendicular to the strain and zigzag direction, $P \perp \varepsilon ||zz$, only the $2D^+$ peak component is selected, which is the case for the green data points. Because no polarization analyzer is used after the sample, both G[±] components are collected with equal intensity (see Supporting Information) and we obtain their average shift, which can be computed as $\Delta \overline{\omega}_{G} = -\omega_{G_0} \gamma_{G} \varepsilon_x (1 - |v|) = -25.1 \varepsilon_x (\text{cm}^{-1}/\%)$. Here we have used graphite's Poisson ratio $\nu = -0.16$, and our previously determined G-band Grüneisen (and shear deformation) parameters 14 $\gamma_G = 1.89$ and $\beta_G = 0.70$, with corresponding linear shift rates for uniaxial strain of $((\partial \omega G^+)/(\partial \varepsilon)) = -18.7$ $(cm^{-1}/\%)$, and $((\partial \omega G^{-})/(\partial \varepsilon)) = -31.5 (cm^{-1}/\%)$.

Using the measured slopes S^{\pm} we can then extract the shift rates for the 2D⁺ and 2D⁻ bands versus uniaxial strain along the zigzag axis: $((\partial \omega_{2D^+})/(\partial \varepsilon)) = S^+ \cdot ((\partial \omega_G)/(\partial \varepsilon)) = -(1.33 \pm 1.3)$ $0.14) \cdot 25.1 (\text{cm}^{-1}/\%) = -33.4 \mp 3.6 (\text{cm}^{-1}/\%) \text{ and } ((\partial \omega_{2D}^{-})/$ $(\partial \varepsilon)$) = S⁻· $((\partial \omega_G)/(\partial \varepsilon))$ = -(2.07 ± 0.36)·25.1(cm⁻¹/%) = -52.0 ∓ 8.9 (cm⁻¹/%). From these values, we can also compute the Grüneisen and shear deformation parameters for the 2D band (again using $\nu = -0.16$), and we find $\gamma_{\rm 2D,zz} = 1.90 \pm 0.21$ and $\beta_{\rm 2D,zz}$ = 0.60 \pm 0.31, very close to the G band values $\gamma_{\rm G}$ = 1.89 and β_G = 0.70. We note that these results are obtained for strain along the zigzag direction and might not apply to strain along the armchair lattice orientation due to the double resonance mechanism and its dependence on lattice direction (and laser energy). Reported values from the literature of all the parameters just discussed are tabulated in the Supporting Information. The variation in the reported shift rates for the 2D band is most likely due to arbitrary lattice directions relative to the strain orientation, the issue of calibrating strain (and

slippage), and the choice of what Poisson ratio should be used (graphene or substrate).

From the analysis above, we also find that the graphene region on the flat substrate is compressed ($\varepsilon = -0.11 + 0.02\%$) and has a charge density between $2-4 \times 10^{12}$ cm⁻². Such unintentional doping level is typical for graphene on SiO₂. Spontaneous graphene compression has been observed previously after heating, ^{24,34,35} and in our sample, it is likely a result of the heating step of the pick-and-place align-transfer process. The graphene region on the grating is found to have a lower charge doping and charge variation <1 × 10¹² cm⁻², as inferred from the location and spread around the fitted lines of slope S^{\pm} . The violet data points are from the second graphene flake on the same grating, measured with polarization along the strain direction (Supporting Information). We see that the slope is the same but the data points are shifted slightly to the right, indicating a slightly larger charge density.

Next, we turn our attention to estimating the strain variation within a period of the corrugated graphene over the grating based on Raman measurements with a linearly polarized 514nm-wavelength laser having a spot size of 0.63 um (Supporting Information, Figure S2). As discussed above, with good clamping the strain should vary sinusoidally around its average value with period $\Lambda_0 = 400$ nm (i.e., the grating period). Because Λ_0 is smaller than the beam size of the laser (0.63 μ m), we cannot directly map out these sinusoidal strain oscillations. However, any strain variation within the laser spot leads to a convoluted Raman peak and, therefore, can be estimated from the resulting increase in Raman line width. To that purpose, we use the G⁻ band in order to start from the narrowest possible peak to better ascertain the line width broadening. The Gmode can be exclusively selected by controlling the polarization of the incoming and scattered light. 30

Figure 4 shows an optical image of the larger graphene flake, and the G- Raman shift and line width measured as a function of position in the line scan indicated by the white horizontal line. As in the 2D strain map of Figure 2, the strain transition region outside the grating is clearly visible, as is the moderate strain variation along the grating. Using the slope information from Figure 3 and our previously determined Grüneisen and shear deformation potential values ¹⁴ (giving $((\partial \omega_G^-)/(\partial \varepsilon))$ = $-31.5(\text{cm}^{-1}/\%)$, we obtain the compression on the flat substrate and the tensile strain on the grating indicated on the right-hand axis of Figure 4b. Figure 4c shows the corresponding G⁻ line width values. We separate these line width data points into three groups: from the more conformed regions over the grating (red), from the less conformed regions (green), and from the flat substrate region (blue). The same color scheme is also used in the colored bands of Figure 4b. On the basis of these data, we find that there is a correlation between strain and line width, which becomes clearer in the cumulative distribution function (CDF) plot of Figure 5a. By generating the CDF of the G-line width from each one of the three groups above, we find three relatively distinct regimes corresponding to different strain conditions. The CDF plots are fitted with a gamma function, and the derivative gives the Gaussian position and width. The corresponding histograms and Gaussian fits are shown in Supporting Information Figure S7. As expected, the more conformed and more highly strained corrugated graphene has the broadest average line width (9.46 cm⁻¹), flat graphene has the narrowest average line width (8.58 cm⁻¹), and the less strained corrugated graphene has an average line width in between these two limits (9.12 cm⁻¹).

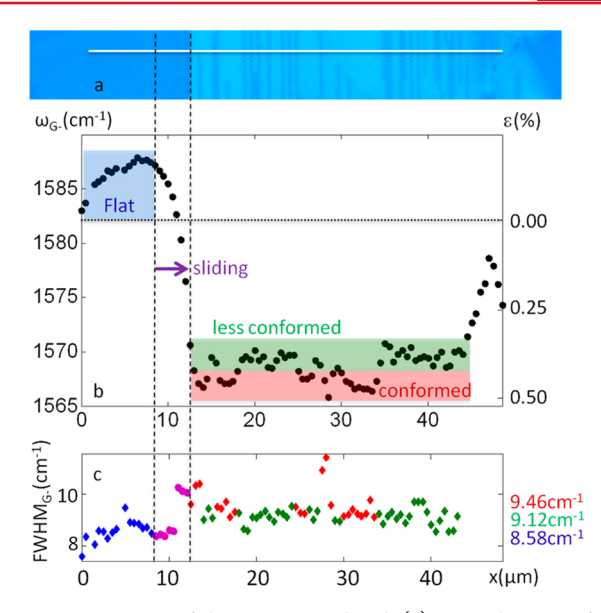


Figure 4. Line scan of the Raman G^- band. (a) Optical image of the graphene flake. (b) G^- peak center versus position along the white line in (a). (c) G^- line width versus position along the same line. The blue, green, and red boxes in (b) correspond to graphene on a flat surface (under compression), partially suspended graphene over the grating (under low tensile strain), and highly conformed graphene over the grating (under higher tensile strain), respectively. The same color scheme is used for the data points in (c).

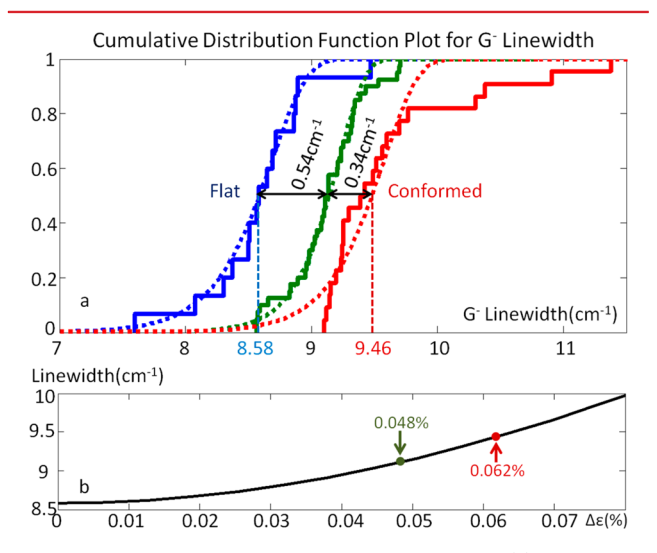


Figure 5. Statistical analysis of the G^- Raman data. (a) Cumulative distribution function (CDF) plot of the G^- line widths measured with the three data sets in Figure 4c: flat graphene (blue), partially suspended graphene (green), and highly conformed graphene (red). The data are fitted with the error function giving the average line widths 8.58 ± 0.42 cm⁻¹, 9.12 ± 0.29 cm⁻¹, and 9.46 ± 0.36 cm⁻¹, respectively. (b) Calculated G^- line width broadening caused by sinusoidal strain oscillations within the laser spot, as a function of the peak-to-peak strain variation. The indicated strain values correspond to the measured average line widths from (a).

These results are then used to estimate the local strain gradient in the corrugated graphene by convolving a sinusoidal strain oscillation of period $\Lambda_0=400$ nm with a Gaussian laser beam of width 626 nm. The resulting G^- line broadening calculated as a function of the strain peak-to-peak variation $\Delta\varepsilon$ is plotted in Figure 5b, where we have taken the value of 8.58 cm⁻¹ measured from the flat substrate region as the $\Delta\varepsilon=0$

baseline. If we attribute 100% of the measured line broadening to strain variations, we find from this plot that in the conformed graphene regions $\Delta \varepsilon = 0.062\%$, as indicated by the red point in Figure 5b. The corresponding strain variation per unit length is $((\Delta \varepsilon)/(0.5\Lambda)) = ((0.062\%)/(0.2 \ \mu m)) = 0.31(\%/\mu m)$ for an average strain $\overline{\varepsilon} \approx 0.5\%$ (from the red band of Figure 4b). This value is substantially lower than the estimate from the perfect clamping model discussed above, $((4\overline{\varepsilon})/(\Lambda_0)) = 5(\%/\mu m)$, which demonstrates once again that graphene slides significantly to redistribute strain. For an absolute upper limit of the strain variation, we should use 6.5 cm⁻¹ (pristine graphene)²¹ as the $\Delta \varepsilon = 0$ baseline in Figure 5b. The same procedure above would then yield $\Delta \varepsilon = 0.11\%$ in the conformed corrugated graphene, corresponding to a strain gradient of 0.55 %/µm (still much smaller than the geometric estimate). In any case, we can argue that this upper limit significantly overestimates the strain contribution to the line width because of the difference in charge on the flat substrate and the grating (Figure 3). With Fermi energy $E_{\rm F}$ within or close to \pm (($|E_{\rm G}|$)/2), G phonons decay into electronic excitations causing a broader homogeneous line width²¹ of up to \sim 16 cm⁻¹. On the basis of the measured charge density, the estimated Fermi level position for the corrugated graphene in our sample is ~ -0.15 eV, close to \pm (($|E_G|$)/2) = 0.1 eV, whereas $|E_F|$ > 0.2 for the flat graphene. Hence, the homogeneous line width on the grating could be even larger than 8.58 cm⁻¹, which would result in a smaller strain variation than the value of 0.062% estimated here.

Finally, to evaluate the role of friction on the measured strain distribution, we analyze a continuum mechanics model of the graphene/SiO₂ system. Full details of the model, including justifications for its various assumptions, are contained in the Supporting Information, and here, we only present the resulting simple equation for graphene in mechanical equilibrium on a flat surface subject to friction forces. The basic idea is to balance friction and elastic forces. In the present sample, there are two regions where such an analysis is easily implemented: the \sim 3 μ m long regions on the left and right sides of the grating where the strain transitions from compression to high tension. In these regions, the equation for mechanical equilibrium is

$$\partial_x \epsilon^{xx} \pm (1 - \nu^2) \frac{f}{tE} = 0 \tag{1}$$

where the x coordinate is taken perpendicular to the grating lines, ε is the strain tensor, f is the shear stress due to friction, and E, ν , and t are the Young's modulus, Poisson's ratio, and thickness of graphene, respectively. The minus sign is taken when the longitudinal displacement of graphene is positive (on the left edge of the sample), and the plus sign is taken when the displacement is negative (on the right edge of the sample). According to this simple model, the strain is therefore a function of position and has a local slope equal to $((\Delta\varepsilon)/(\Delta x)) = \pm (((1-\nu^2)f)/(tE))$. For the transition region on the right side, optical inspection and Raman analysis indicate that the graphene flake is a bilayer. Hence, we expect the local slope there to be cut in half based on its thickness dependence, as clearly observed in Figure 4b.

Using eq 1, we extract the friction f from the measured local slope $((\Delta \varepsilon)/(\Delta x))$ for both bilayer and single layer graphene (from Figure 4), and the results are plotted versus the corresponding strain values in Figure 6. The double layer is anchored on the grating, not the flat substrate, but there is no observed difference in friction. This demonstrates that the gentle grating corrugation does not affect the friction for single

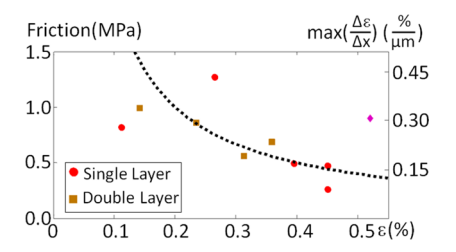


Figure 6. Estimated friction versus strain. The line $f \propto 1/\varepsilon$ is the same as used in earlier work. ¹⁴ The corresponding values of $((\Delta\varepsilon)/(\Delta x))$ are marked on the right-hand side. The purple diamond data point on the right shows the maximum strain variation predicted from the line width broadening calculation.

and bilayer graphene. In general, the friction behavior for monolayer and bilayer graphene is very similar, and it is only when the thickness increases to trilayer and beyond that the bending rigidity due to the local microscopic corrugation begins to have an impact.¹⁴ Hence, it is reasonable to assume that the grating corrugation does not affect the friction in our monolayer and bilayer sample. As a guide to the eye, a line proportional to $1/\varepsilon$ is also plotted in Figure 6 (exactly the same line 14 used for pressurized graphene on SiO₂), showing a very good agreement. On the right axis in Figure 6 we have also indicated the corresponding value of $((\Delta \varepsilon)/(\Delta x))$ (for monolayer graphene) versus ε , to highlight that there is a maximum strain variation per unit length that can be sustained by the substrate friction. The data point based on the upper strain variation estimate from the G⁻ line width, 0.31% strain/ μ m, is also included in this plot (purple diamond), consistent with the elastic analysis, albeit on the high side for the reasons discussed above. The decrease in friction with increasing strain observed in Figure 6 can be explained as a result of decreasing surface contact area. For zero strain, graphene can conform very well to the underlying substrate surface morphology, including any microscopic roughness. 18 Strain, however, smooths out the graphene sheet¹⁴ and, hence, reduces the contact area. Such strain dependence of the friction clamping could be an issue for strain engineered devices, although it could be reduced with a flatter substrate surface.

The pick-and-place method does not yield graphene as clean as directly exfoliated graphene, and polymer residue could alter the friction between graphene and SiO_2 . Because the friction values in Figure 6 are comparable to the friction between directly exfoliated graphene and SiO_2 . ¹⁴ any contamination that might be present does not change the friction substantially.

In summary, we have shown that graphene slides on a SiO₂ surface to redistribute strain. Elastic analysis of the strain transition region for single- and double-layer graphene gives consistent values of the maximum strain per unit length before this redistribution takes place, as a function of the friction between graphene and SiO₂. A decreased clamping with increasing strain is also observed, which is associated with the use of naturally microscopically rough SiO₂ substrates. It is possible that the use of microscopically flatter substrates could mitigate this decrease in friction, which may have potential applications in strain engineering. In contrast, the slowly varying corrugation of the grating $((A/\Lambda_0) < 0.14)$ used in this work has no effect on the friction. The limited line width broadening of the strained graphene on the grating shows that local variation within a lattice spacing is an order of magnitude smaller than would be expected from perfect clamping. This also demonstrates sliding and strain redistribution when the

friction force is not high enough to clamp the graphene sheet. Altogether, these results are important for evaluating maximum strain and strain gradients in any strain engineering devices. In addition, we have used statistics of the 2D to G band positions to separate the charge and strain contributions to the Raman peak shifts. The use of uniaxial strain in the zigzag direction has also allowed us to extract the Grüneisen parameter and shear deformation potential for the $2D^\pm$ peaks, which were found to be close to the G band values.

ASSOCIATED CONTENT

S Supporting Information

The Supporting Information is available free of charge on the ACS Publications website at DOI: 10.1021/acs.nanolett.5b02107.

Additional information on pick-and-place transfer method, lattice orientation determination from polarized Raman spectroscopy, geometric strain calculation and sinusoidal strain variation, Gaussian beam determination, strain convolution, 2D/G charge slope, line scans from other samples, and elastic model. (PDF)

AUTHOR INFORMATION

Corresponding Author

*E-mail: swan@bu.edu.

Author Contributions

KT made the SiO₂ gratings directed by RP, XW made the graphene transfers and performed the AFM and Raman measurements and data analysis, JC performed the elasticity analysis, XW and AKS wrote the manuscript with input from all coauthors, AKS directed the experimental measurements.

Notes

The authors declare no competing financial interest.

■ ACKNOWLEDGMENTS

The authors gratefully acknowledge support from the United States National Science Foundation (DMR 1411008, DMR 1308659) and a Boston University Dean's Catalyst Award. JWC gratefully acknowledges a Department of Defense NDEG fellowship.

REFERENCES

- (1) Geim, A. K.; Novoselov, K. S. Nat. Mater. 2007, 6, 183-191.
- (2) Kim, K. S.; Zhao, Y.; Jang, H.; Lee, S. Y.; Kim, J. M.; Kim, K. S.; Ahn, J.-H.; Kim, P.; Choi, J.-Y.; Hong, B. H. *Nature* **2009**, *457*, 706–710.
- (3) Lee, C.; Wei, X.; Kysar, J. W.; Hone, J. Science 2008, 321, 385–388.
- (4) Kim, B. J.; Jang, H.; Lee, S.-K.; Hong, B. H.; Ahn, J.-H.; Cho, J. H. Nano Lett. **2010**, *10*, 3464–3466.
- (5) Pereira, V. M.; Castro Neto, A. H. Phys. Rev. Lett. 2009, 103, 046801.
- (6) Pereira, J. M., Jr; Mlinar, V.; Peeters, F. M.; Vasilopoulos, P. Phys. Rev. B: Condens. Matter Mater. Phys. 2006, 74, 045424.
- (7) Zhao, X.; Zhai, X.; Zhao, A.; Wang, B.; Hou, J. G. Appl. Phys. Lett. 2013, 102, 201602.
- (8) Lee, J.-K.; Yamazaki, S.; Yun, H.; Park, J.; Kennedy, G. P.; Kim, G.-T.; Pietzsch, O.; Wiesendanger, R.; Lee, S.; Hong, S. *Nano Lett.* **2013**, *13*, 3494–3500.
- (9) Guinea, F.; Geim, A. K.; Katsnelson, M. I.; Novoselov, K. S. Phys. Rev. B: Condens. Matter Mater. Phys. 2010, 81, 035408.
- (10) Levy, N.; Burke, S. A.; Meaker, K. L.; Panlasigui, M.; Zettl, A.; Guinea, F.; Neto, A. C.; Crommie, M. F. Science **2010**, 329, 544–547.

- (11) Bunch, J. S.; Van Der Zande, A. M.; Verbridge, S. S.; Frank, I. W.; Tanenbaum, D. M.; Parpia, J. M.; Craighead, H. G.; McEuen, P. L. Science **2007**, *315*, 490–493.
- (12) Chen, C.; Rosenblatt, S.; Bolotin, K. I.; Kalb, W.; Kim, P.; Kymissis, I.; Stormer, H. L.; Heinz, T. F.; Hone, J. *Nat. Nanotechnol.* **2009**, *4*, 861–867.
- (13) Zhang, K.; Arroyo, M. J. Appl. Phys. 2013, 113, 193501.
- (14) Kitt, A. L.; Qi, Z.; Rémi, S.; Park, H. S.; Swan, A. K.; Goldberg, B. B. *Nano Lett.* **2013**, *13*, 2605–2610.
- (15) Lee, C.; Wei, X.; Li, Q.; Carpick, R.; Kysar, J. W.; Hone, J. *Phys. Status Solidi B* **2009**, 246, 2562–2567.
- (16) Scharfenberg, S.; Rocklin, D. Z.; Chialvo, C.; Weaver, R. L.; Goldbart, P. M.; Mason, N. Appl. Phys. Lett. **2011**, 98, 091908.
- (17) Koenig, S. P.; Boddeti, N. G.; Dunn, M. L.; Bunch, J. S. Nat. Nanotechnol. **2011**, *6*, 543–546.
- (18) Cullen, W. G.; Yamamoto, M.; Burson, K. M.; Chen, J. H.; Jang, C.; Li, L.; Fuhrer, M. S.; Williams, E. D. *Phys. Rev. Lett.* **2010**, *105*, 215504.
- (19) Tantiwanichapan, K.; DiMaria, J.; Melo, S. N.; Paiella, R. Nanotechnology 2013, 24, 375205.
- (20) Pisana, S.; Lazzeri, M.; Casiraghi, C.; Novoselov, K. S.; Geim, A. K.; Ferrari, A. C.; Mauri, F. Nat. Mater. **2007**, *6*, 198–201.
- (21) Yan, J.; Zhang, Y.; Kim, P.; Pinczuk, A. Phys. Rev. Lett. 2007, 98, 166802.
- (22) Casiraghi, C.; Pisana, S.; Novoselov, K. S.; Geim, A. K.; Ferrari, A. C. Appl. Phys. Lett. **2007**, *91*, 233108.
- (23) Das, A.; Pisana, S.; Chakraborty, B.; Piscanec, S.; Saha, S. K.; Waghmare, U. V.; Novoselov, K. S.; Krishnamurthy, H. R.; Geim, A. K.; Ferrari, A. C. *Nat. Nanotechnol.* **2008**, *3*, 210–215.
- (24) Lee, J. E.; Ahn, G.; Shim, J.; Lee, Y. S.; Ryu, S. Nat. Commun. 2012, 3, 1024.
- (25) Seidel, H.; Csepregi, L.; Heuberger, A.; Baumgärtel, H. *J. Electrochem. Soc.* **1990**, *137*, 3612–3626.
- (26) Marcus, R. B.; Sheng, T. T. J. Electrochem. Soc. 1982, 129, 1278–1282.
- (27) Dean, C. R.; Young, A. F.; Meric, I.; Lee, C.; Wang, L.; Sorgenfrei, S.; Watanabe, K.; Taniguchi, T.; Kim, P.; Shepard, K. L. *Nat. Nanotechnol.* **2010**, *5*, 722–726.
- (28) Chen, H.; Yao, Y.; Chen, S. J. Phys. D: Appl. Phys. 2013, 46, 205303.
- (29) Shi, Y.; Dong, X.; Chen, P.; Wang, J.; Li, L.-J. Phys. Rev. B: Condens. Matter Mater. Phys. 2009, 79, 115402.
- (30) Huang, M.; Yan, H.; Heinz, T. F.; Hone, J. Nano Lett. **2010**, 10, 4074–4079.
- (31) Frank, O.; Mohr, M.; Maultzsch, J.; Thomsen, C.; Riaz, I.; Jalil, R.; Novoselov, K. S.; Tsoukleri, G.; Parthenios, J.; Papagelis, K. ACS Nano 2011, 5, 2231–2239.
- (32) Mohr, M.; Maultzsch, J.; Thomsen, C. Phys. Rev. B: Condens. Matter Mater. Phys. 2010, 82, 201409.
- (33) Berciaud, S.; Li, X.; Htoon, H.; Brus, L. E.; Doorn, S. K.; Heinz, T. F. *Nano Lett.* **2013**, *13*, 3517–3523.
- (34) Chen, C.-C.; Bao, W.; Chang, C.-C.; Zhao, Z.; Lau, C. N.; Cronin, S. B. *Phys. Rev. B: Condens. Matter Mater. Phys.* **2012**, 85, 035431.
- (35) Ryu, S.; Liu, L.; Berciaud, S.; Yu, Y.-J.; Liu, H.; Kim, P.; Flynn, G. W.; Brus, L. E. *Nano Lett.* **2010**, *10*, 4944–4951.
- (36) Mohiuddin, T. M. G.; Lombardo, A.; Nair, R. R.; Bonetti, A.; Savini, G.; Jalil, R.; Bonini, N.; Basko, D. M.; Galiotis, C.; Marzari, N. *Phys. Rev. B: Condens. Matter Mater. Phys.* **2009**, *79*, 205433.